WILEY

RESEARCH ARTICLE

A quad-band bandpass filter using sept-mode double square-ring loaded resonator

Bao-Hua Zhu | Zhi-Ji Wang | Eun-Seong Kim | Nam-Young Kim

RFIC Center, Kwangwoon University, Seoul, Korea

Correspondence
Nam-Young Kim, RFIC Center, Kwangwoon University, 447-1 Wolgye-Dong, Nowon-Ku, Seoul 139-701, Korea.
Email: nykim@kw.ac.kr

Abstract

A quad-band bandpass filter (BPF) using a sept-mode double square-ring loaded resonator (DSRLR) is presented in this article. Based on the symmetrical geometric construction of the DSRLR, the even- and odd-mode analysis with theoretical equations is employed to analyze the proposed BPF, and current density are obtained. Additionally, multimode splitting and resonant characteristics of the proposed DSRLR are explored. Accordingly, the design procedure is given after a pair of feedlines with dual-finger structure is added to the I/O ports to introduce extra transmission zeros (TZs). Four TZs—including two created by the dual-finger feedlines—are produced to separate four passbands that exhibit a sharp skirt and high stopband rejection. Finally, a microstrip quad-band BPF is fabricated on a Teflon substrate with four measured passbands centered at 2.46, 3.41, 6.65, and 9.09 GHz with insertion losses of 0.68, 0.73, 0.81, and 1.23 dB, respectively. A satisfactory agreement is achieved between the measurement results and full-wave simulation results.

KEYWORDS

bandpass filter, double square-ring loaded resonators, microstrip, quad-band, sept-mode

1 | INTRODUCTION

With developments in modern intelligent technology (such as the Internet of things [IoT] and self-driving systems), the demand for wireless communication modules—indispensable components for the transmission of intelligent device information—is increasing significantly.[1] As a pivotal passive block of the RF front-end of the multiservice wireless operation system, the multiband bandpass filter (BPF) has received widespread attention.[2]

Recently, a variety of quad-band BPFs utilizing diverse fabrication techniques have been reported.[3-7] A miniaturized quad-band BPF (based on a pair of coupled structures with a multimode split ring resonator (SRR) and an asymmetric stepped impedance resonator [SIR]) and another compact second-order quad-band filter (consisting of a set of coupled quadruple-mode square-ring loaded structures with meander coupled lines and pseudo-interdigital coupling structures) were fabricated utilizing a high-temperature superconducting substrate.[3,4] Each has the advantages of low insertion loss (IL) and compact size, but strict requirements for operating conditions. A miniature quad-band BPF that combines four basic resonator types (outer-frame, defected ground structures [DGS], U-shaped resonator, and modified end-coupled microstrip line) on a $MgTa_{1.5}Nb_{0.5}O_6$ microwave ceramic substrate is developed in Reference 5 with improved selectivity by introducing several transmission zeros (TZs). However, its fabrication process is complicated. By combining the multimode resonator theory and single-/dual-band synthesis method, a compact multiband filter in a substrate-integrated waveguide (SIW) with high selectivity is investigated in Reference 6. However, the measured ILs are greater than 2 dB. In Reference 7, another multiband BPF with numerous in-band TZs is achieved using an E-plane septa, but the IL is moderate.

Moreover, owing to the advantages of lower cost, easier fabrication, and flexible multiband design approach, the microstrip quad-band BPF based on the hybrid substrate has attracted much attention as the focus of a large number of studies.[8-11] For example, Reference 8 proposes a microstrip quad-band BPF constructed by introducing improved coplanar waveguide (CPW)-fed and the DGS via dual-mode perturbations with dual-mode double square-ring resonators to achieve high out-of-band rejection and low IL. In Reference 9, a fast design approach using spiral-shaped $\lambda_g/2$ resonators

and spaced apart by $\lambda_g/4$ was employed to implement quad-band BPF with the merit of flexible multiband design, ultrawide band, and controllable TZs. As two common resonators employing to achieve multiband design, stub-loaded resonator (SLR) and SIR were also utilized in the quad-band BPF implementation. A compact quad-band BPF combined a multi-SLR and a short-end SLR was realized in Reference 10 via coupling stubs with an advantage of four individually controllable passbands. And in Reference 11, a quad-mode SIR was proposed and a quad-band BPF was designed with a pair of half-wavelength inter-coupled quad-mode SIRs and two open-loop SIRs, which also providing flexible design procedure. Besides these resonators mentioned above, ring resonators, such as single ring resonator, square-ring loaded resonator (SRLR), are also popularly utilized in multiband BPF design and implementation.[12,13] Nevertheless, to our knowledge, multimode ring resonator-based quad-band BPF on the hybrid substrate is barely reported.

In this study, a novel double square-ring loaded resonator (DSRLR) that possesses seven resonant modes (RMs) is reported, theoretically analyzed, and experimentally verified. The proposed DSRLR is based on an SRLR, that has only one square-ring structure located at one side. However, the proposed DSRLR is constructed by loading two asymmetric square-ring structures of different dimensions on both sides of a transmission line. The effect of the position of these two loaded square-ring at the middle transmission line on the RMs is discussed via the simulation for the first time. A quad-band BPF is proposed using the sept-mode DSRLR and a pair of dual-finger feedlines that features four passbands centered at 2.46, 3.41, 6.65, and 9.09 GHz with 3 dB fraction bandwidths (FBW) of 6.9%, 3.5%, 5.0%, and 4.7%, respectively. Additionally, four TZs are produced to separate the four passbands and guarantee high skirt selectivity. The resonance characterization of the DSRLR is theoretically analyzed by even- and odd-mode theory and current density, which are introduced in Section 2. The multimode splitting and resonant characteristics are also presented in Section 2. In Section 3, the quad-band BPF is simulated and fabricated on a Teflon substrate to verify the theoretical analysis.

2 | RESONATOR ANALYSIS

2.1 | Resonator analyses

2.1.1 | Even-mode and odd-mode

Figure 1 shows a geometrical schematic of the sept-mode DSRLR. It primarily consists of two combined square-ring resonators of different dimensions and two short open-end stubs, where (L_1, W_1) are the length and width of the stubs, and $(2L_2 + 2L_4 + 2L_5, W_1)$ and $(2L_3 + 2L_5, W_1)$ are the dimensions of the upper and lower loaded square-ring, respectively. The
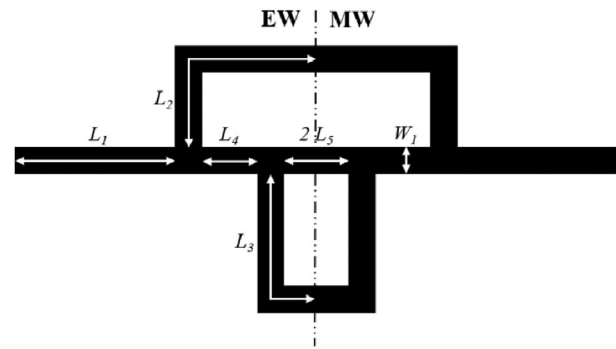

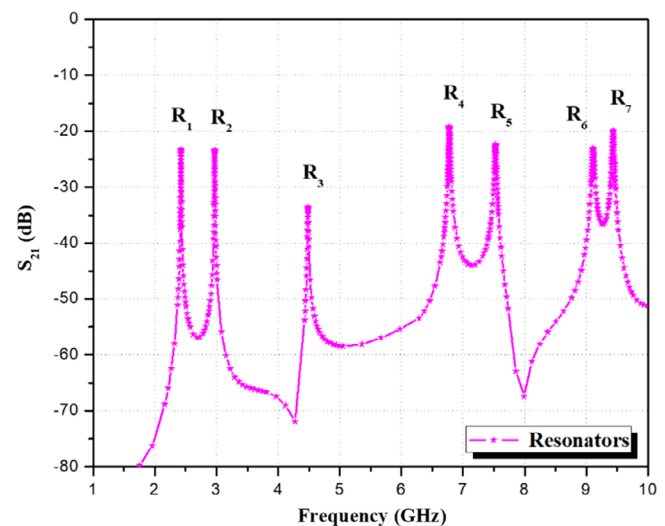**FIGURE 1** Schematic diagram of the proposed sept-mode resonator

FIGURE 2 Frequency response of the proposed resonator [Color figure can be viewed at wileyonlinelibrary.com]

simulation result for the DSRLR—with I/O ports coupled with two 50 Ω impedance match—is plotted in Figure 2. It is evident that seven RMs operate in the frequency range from 0 to 10 GHz. Due to the symmetrical construction, the proposed DSRLR can be characterized by the even- and odd-mode analysis method. The equivalent circuit under even-mode excitation is shown in Figure 3A with the symmetrical plane modeled as the magnetic wall. The equivalent circuit depicted in Figure 3B illustrates the odd-mode resonance condition in which the symmetrical plane is equivalent to the electric wall. Here, $Y_{\text{in-even}}$ and $Y_{\text{in-odd}}$ denote the input admittance of the even-mode equivalent circuit and odd-mode equivalent circuit, respectively; and Y_0 is the characteristic admittance regarding the transmission line. According to transmission line theory, $Y_{\text{in-even}}$ and $Y_{\text{in-odd}}$ can be deduced by:

$$Y_{\text{in}-\text{even}} = Y_0 \frac{jY_0\tan\theta_1 + jY_0\tan\theta_2 + jY_0\tan\theta_4 + Q_{\text{even}}}{Y_0 - j\tan\theta_1(\tan\theta_2 + \tan\theta_4 + Q_{\text{even}})} \quad (1)$$

$$Y_{\text{in}-\text{odd}} = jY_0 \frac{jY_0\tan\theta_1 - jY_0\cot\theta_2 - jY_0\cot\theta_4 + Q_{\text{odd}}}{Y_0 - j\tan\theta_1(-jY_0\cot\theta_2 - jY_0\cot\theta_4 + Q_{\text{odd}})} \quad (2)$$

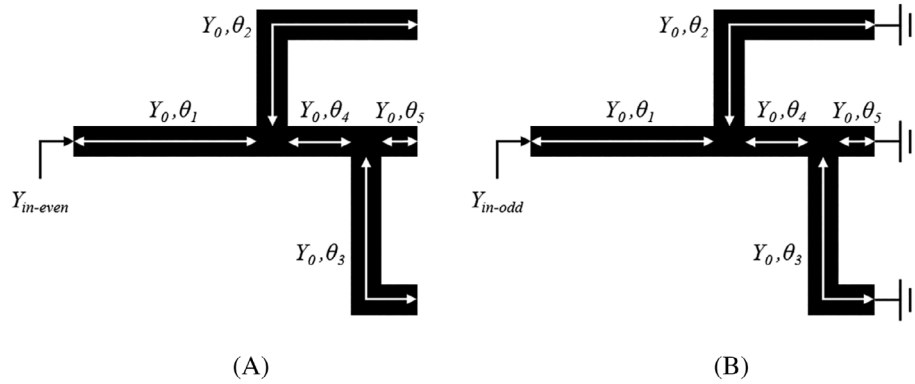**FIGURE 3** Equivalent circuit of the proposed resonator under A, even-mode and B, odd-mode

where:

$$Q_{even} = Y_0 \frac{jY_0\tan\theta_3 + jY_0\tan\theta_4 + jY_0\tan\theta_5}{Y_0 + j\tan\theta_4(jY_0\tan\theta_3 + jY_0\tan\theta_5)} \quad (3)$$

$$Q_{odd} = Y_0 \frac{jY_0\tan\theta_4 - jY_0\cot\theta_3 - jY_0\cot\theta_5}{Y_0 + \tan\theta_4(-jY_0\cot\theta_3 - jY_0\cot\theta_5)} \quad (4)$$

where is the electronic length of each transmission lines, $\theta_1 = \beta L_1$, $\theta_2 = \beta L_2$, $\theta_3 = \beta L_3$, $\theta_4 = \beta L_4$, $\theta_5 = \beta L_5$, and $\beta = 2\pi/\lambda_g$ is the propagation constant. The even- and odd-mode resonances are excited when the input admittance equals zero at the operating resonant frequency. Put differently, the even-mode resonance is excited when $Y_{in\text{-}even} = 0$, and the odd-mode resonance is excited when $Y_{in\text{-}odd} = 0$. Therefore, the resonance condition of even-modes and odd-modes of the proposed DSRLR can be derived as follows:

$$\tan\theta_1 + \tan\theta_2 + \tan\theta_4 + \frac{\tan\theta_3 + \tan\theta_4 + \tan\theta_5}{1 - \tan\theta_4(\tan\theta_3 + \tan\theta_5)} = 0 \quad (5)$$

$$\tan\theta_1 - \cot\theta_2 - \cot\theta_4 + \frac{\tan\theta_4 - \cot\theta_4 - \cot\theta_5}{1 + \tan\theta_4(\cot\theta_3 + \cot\theta_5)} = 0 \quad (6)$$

2.1.2 | Current density

In Figure 2, seven RMs of the proposed DSRLR are distributed at 2.42, 2.97, 4.48, 6.77, 7.52, 9.11, and 9.46 GHz. The DSRLR current density is calculated by simulation software and indicated in Figure 4. According to even- and odd-mode theory (and Figure 3), the symmetrical plane of the DSRLR behaves as a magnetic wall and electric wall under even- and odd-mode excitation, respectively. When the symmetrical plane is under even-mode excitation, the charges distributed in two bisections of the DSRLR possess the same polarity, and the half bisection acts as the open-end circuit. Under odd-mode excitation, the polarity of the charges is opposite. As such, the half bisection is equivalent to the short-end and the symmetrical plane acts as the virtual ground. Therefore, the resonances operating at 2.42, 6.77, and 9.11 GHz—as shown in Figure 4A,D,F, respectively—do so under even-mode excitation, whereas the resonances
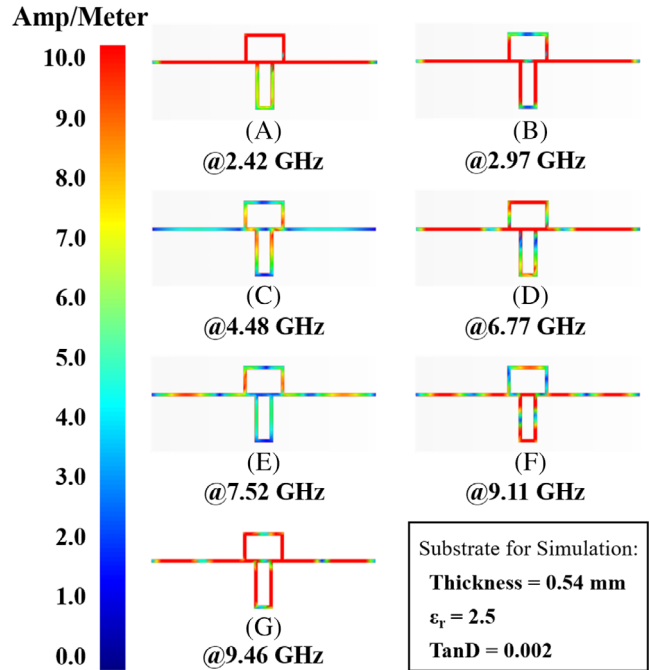

FIGURE 4 Simulated current density of resonator at: A, 2.42 GHz; B, 2.97 GHz; C, 4.48 GHz; D, 6.77 GHz; E, 7.52 GHz; F, 9.11 GHz; and G, 9.46 GHz [Color figure can be viewed at wileyonlinelibrary.com]

operating at 2.97, 4.48, 7.52, and 9.46 GHz—as shown in Figure 4B,C,E,G, respectively—do so under odd-mode excitation. The simulation substrate parameters are also shown in Figure 4.

2.2 | Multi-mode splitting and resonant characteristics

Different from previous ring-resonator, the RM generated by two square-ring structure with different dimension in the DSRLR can be affected each other. Therefore, variations in the resonant frequencies with adjustments to the geometrical parameters L_2, L_3, L_4, and L_5 are plotted in Figure 5 to clarify the multimode splitting and RM shifting. As shown in Figure 5A, R_3, R_4, R_5, and R_7 move toward the lower
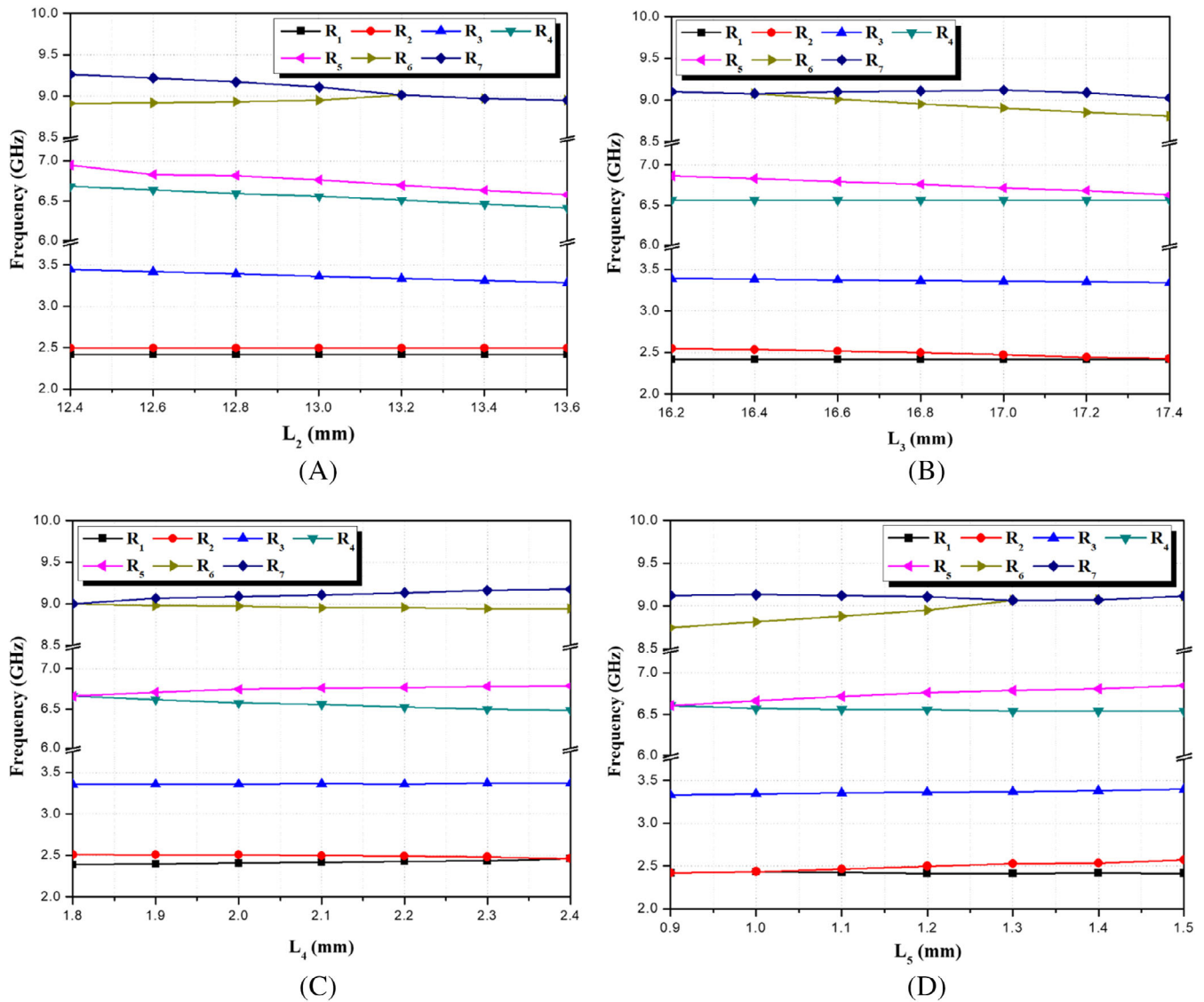
FIGURE 5 Variation trends of the seven resonant frequencies of the proposed structure with the values of A, L_2; B, L_3; C, L_4; and D, L_5 [Color figure can be viewed at wileyonlinelibrary.com]

frequency with each increment of L_2, whereas the other RMs remain stable. When L_3 increases from 16.2 to 17.4 mm, R_2 shifts left slightly, and R_5 and R_7 shift left significantly; the other RMs remain unchanged, as shown in Figure 5B. Moreover, as revealed in Figure 5C, R_1 increases slightly and finally merges with the R_2. Meanwhile, R_4 and R_5, the R_6 and R_7 split when L_4 increases from 1.8 to 2.4 mm. In Figure 5D, when L_5 increases from 0.9 to 1.5 mm, R_2 shifts slightly while R_5 and R_6 exhibit visible shifts to higher frequencies.

According to Equations (5) and (6) and the above analysis, R_1 is determined by ($L_1 + L_4 + L_5$); R_2 is determined by L_3 and L_5; R_3 and R_6 are only affected by L_2 and L_3, respectively; R_4 and R_7 are each determined by L_2 and L_4; and R_5 can be affected by a dimension change to any transmission line.

2.3 | Quad-band BPF design

In order to achieve good response of each passband during quad-band BPF implementation, the 3-dB bandwidth and the external quality factor (Q_e) vs varying geomatical size are analyzed and simulated as well, which are revealed in Figure 6. The Q_e can be extracted from the following:

$$Q_e = \frac{\omega_0}{\Delta\omega \pm 90°} \tag{7}$$

where ω_0 is the resonant frequency, $\Delta\omega \pm 90°$ is the absolute bandwidth between the $\pm 90°$ points of the S_{11} phase response. As mentioned above, the middle transmission line is firstly decided using a $\lambda_g/2$ resonator to design a quad-band BPF. Two square-rings with different locations, assuming L_2 equal to L_3 first, are loaded at both sides of the transmission line. Afterward, seven RMs are generated
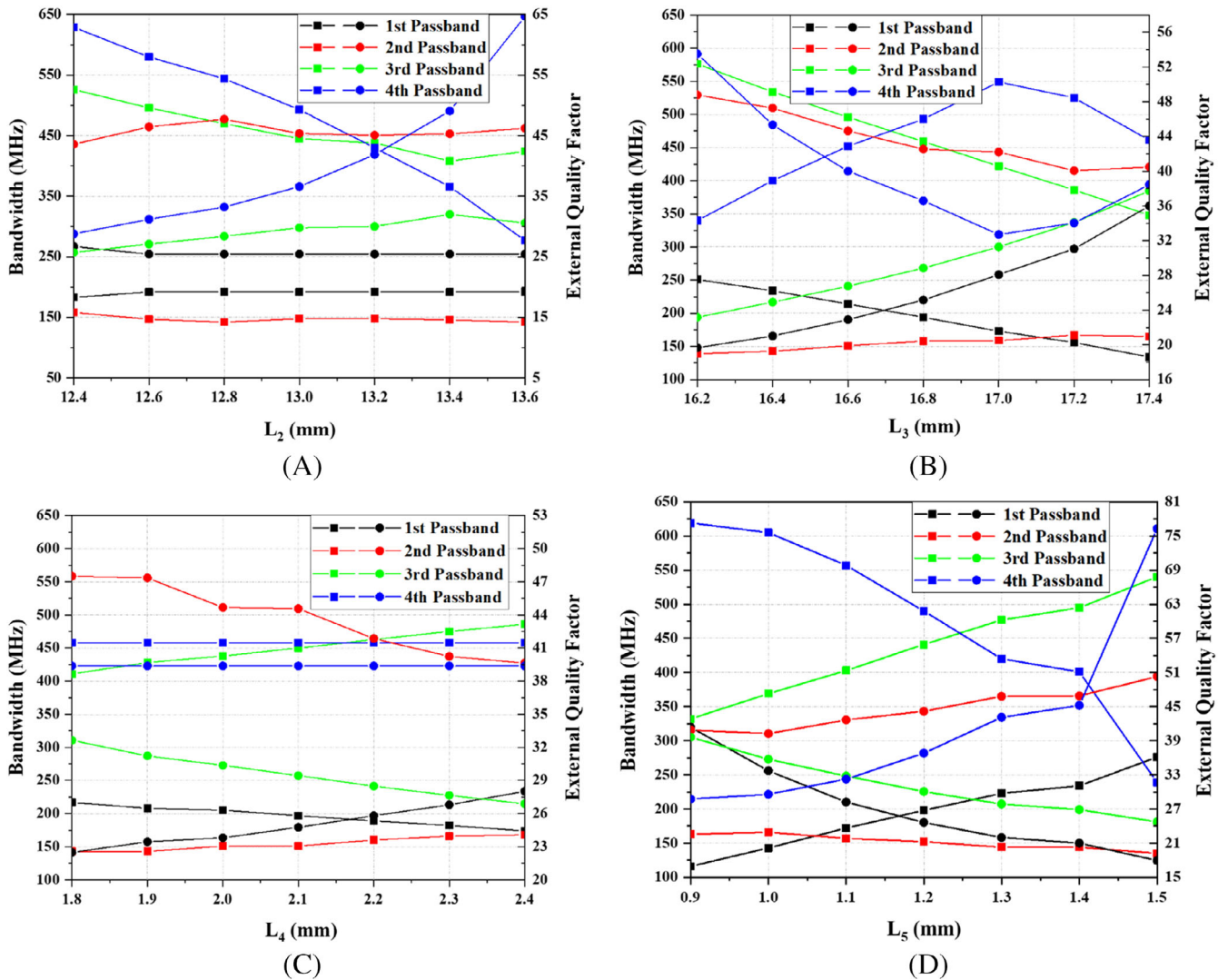
FIGURE 6 The variation of the bandwidth and external quality factor Q_e of the proposed structure with the values of A, L_2; B, L_3; C, L_4; and D, L_5 [Color figure can be viewed at wileyonlinelibrary.com]
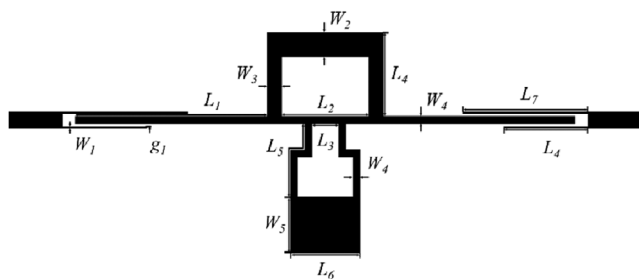

FIGURE 7 Configuration of the quad-band BPF based on the proposed sept-mode resonator

and two TZs are generated between R_2 and R_3, R_5 and R_6. To form four passbands and enhanced the selectivity and band-in-band rejection, the dual-finger coupling line is added to the input and output resulting in two TZs are generated between R_3 and R_4. Then, tuning the length of L_3 shown in Figure 1 to achieve the first passband along with the reduced bandwidth. Next, tuning the length of L_2 to enhances and decrease bandwidth along with the lowered IL resulting in adjusting the fourth passband. Meanwhile, R_3 also will be shifted to close to a TZ resulting in a higher IL, that can be improved from moving the TZ to the lower

TABLE 1 Dimensional parameters of the proposed quad-band BPF

Parameter	L_1	L_2	L_3	L_4	L_5	L_6	L_7	g_1	W_1	W_2	W_3	W_4	W_5
Unit (mm)	17.7	8.0	2.4	7.7	8.6	6.4	11.5	0.2	0.2	2.4	1.3	0.7	5.0

Abbreviation: BPF, bandpass filter.

frequency via enlarging the width of the bottom side of one square-ring, named W_5 in Figure 7. Subsequently, the relative location of two square-ring is adjusted via tuning the length of L_4 to form third and fourth passband and lower the ILs. Additionally, the position of these two square-ring is adapted through the adjustment of the length of L_5 to achieve fourth passband, while the bandwidth and Q_e of third passband are tuned in reverse. Finally, tuning the width of the upper square-ring to get the lowest IL of each passband. Accordingly, the desired quad-band response can be obtained by changing the geometric parameters, L_2, L_3, L_4, and L_5 equal to 13, 16.8, 2.1, 1.2 mm, respectively, to induce a suitable Q_e equal to 25.2, 42.6, 28.4, 36.8.
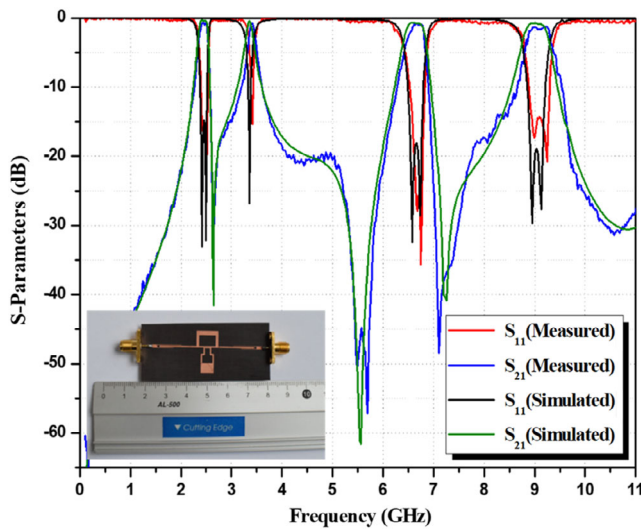

FIGURE 8 Comparison of the simulated and measured results of the quad-band sept-mode BPF with the paragraph of the fabricated device. BPF, bandpass filter [Color figure can be viewed at wileyonlinelibrary.com]

3 | RESULTS AND DISCUSSION

Based on the theoretical analysis and design procedure clarified in Section 2, a quad-band BPF is designed and simulated after adjusting the dimensions and folding the loaded square-ring of the reported sept-mode DSRLR—depicted in Figure 7. The proposed BPF is modeled and simulated by Advanced Design System (ADS) software with a set of dual-finger feedlines attached to the I/O ports. Two TZs are produced between the second and third passbands resulting from the unequal dual-finger feed structure.[14] The exact configuration of the quad-band BPF is listed in Table 1 after optimization with ADS.

To verify the analysis and design of the quad-band BPF further, a device is fabricated using a Teflon substrate with a dielectric constant of 2.5, thickness of 0.54 mm, and tan δ of 0.002, and the S-parameter measurement is performed and recorded by an Agilent 8510C vector network analyzer. A comparison of the ADS simulation and measured results is illustrated in Figure 8. The inset of Figure 8 exhibits the fabricated filter with a size of 46×20.7 mm^2 ($0.59 \lambda_g \times 0.26 \lambda_g$, where λ_g is the guided wavelength at the center frequency of the lower passband). The measured result reveals that the seven RMs of the quad-band BPF operate at 2.43, 2.52, 3.41, 6.67, 6.75, 8.98, and 9.24 GHz. The four passbands are centered at 2.46, 3.41, 6.65, and 9.09 GHz with 3 dB FBWs of 6.9%, 3.5%, 5.0%, and 4.7%, respectively. Furthermore, the measured minimum IL of each passband—with the losses of two SMA connectors—are ~0.68, 0.73, 0.81, and 1.23 dB, while the maximum passband return losses are ~15.1, 15.3, 25.7, and 14.3 dB. Additionally, four TZs are generated at 2.65, 5.48, 5.69, and 7.10 GHz, resulting from the utilization of dual-finger feedlines and from the inherent property of the transversal signal interface among multi-transmission paths.[14] This greatly promotes stopband

TABLE 2 Comparison with the other quad-band works

References	CF(GHz)/FBW	IL (dB)	TZs	Circuit area
Ref. 15 (SIR/SLRs)	2.4/9.9%, 3.5/11.8%, 4.5/6.5%, 5.8/9.9%	1.3/0.9/ 2.2/1.3	9	$0.18 \times 0.27 \lambda_g^2$
Ref. 16 (TLR/SLR)	2.4/6.87%, 3.5/6.1%, 5.2/3.1%, 5.8/1.4%	1.8/1.5/ 2.1/2.9	7	$0.23 \times 0.23 \lambda_g^2$
Ref. 17 (SLCFS)	1.54/11%, 2.45/4.9%, 3.58/8.8%, 5.2/5%	1.9/2.8/ 3.7/4.6	8	Not mentioned
Ref. 18 (SIR/SLR)	0.91/7.9%, 1.47/10.5%, 2.46/5.6%, 3.54/6.3%	1.53/1.31/ 1.43/1.61	3	$0.098 \times 0.085 \lambda_g^2$
Ref. 19 (SLRs)	1.77/3.4%, 3.4/5.4%, 5.28/5.1%, 6.8/4.9%	4.2/2.9/ 3.7/2.6	2	$0.054 \times 0.195 \lambda_g^2$
This work (DSRLR)	2.46/6.9%, 3.41/3.5%, 6.65/5.0%, 9.09/4.7%	0.68/0.73/ 0.81/1.23	4	$0.59 \times 0.26 \lambda_g^2$

Abbreviations: FBW, fraction bandwidth; IL, insertion loss; TZs, transmission zeros.

restriction with the maximum suppression of all stopbands being greater than 30 dB. In particular, the band-in-band suppression between the second and third passbands is greater than 57 dB, while that between the third and fourth passbands is greater than 48 dB. Simultaneously, the selectivity of the BPF is also enhanced with the improvement of the steepness of the slope close to the passband. Comparison between the simulated and measured results presents good agreement, which validates the analysis and design of the reported quad-band BPF. Slight differences between simulated and measured results still exist, which are primarily attributed to fabrication tolerance. A comparison of the proposed quad-band BPF with other previously reported BPFs is given in Table 2. It can be observed that the proposed quad-band BPF exhibits good isolation and favorable selectivity compared with References 15-17. Moreover, compared with References 18 and 19, the proposed BPF exhibits lower IL.

4 | CONCLUSION

A quad-band BPF based on the proposed sept-mode DSRLRs was designed, simulated, and fabricated for multiband wireless operation systems. The DSRLR with two different square-ring structures loaded on both sides of a transmission line was developed and used in the design of a quad-band BPF. Even- and odd-mode theory and current density were employed for resonator characterization. The measured central frequencies of four passbands were located at 2.46, 3.41, 6.65, and 9.09 GHz with low IL of 0.68, 0.73, 0.81, and 1.23 dB, respectively. Additionally, four TZs were generated at 2.65, 5.48, 5.69, and 7.10 GHz, resulting in high selectivity and good stopband isolation. Theoretical prediction was validated by the consistency between simulation and measurement. In general, the proposed BPF is an attractive option for modern multiservice wireless communication systems due to its enhanced selectivity, good band-to-band isolation, and low IL.

ORCID

Bao-Hua Zhu https://orcid.org/0000-0002-4223-250X
Zhi-Ji Wang https://orcid.org/0000-0001-7816-0790

REFERENCES

[1] Chen D, Zhao C, Jiang Z, Shum KM, Xue Q, Kang K. A V-band Doherty power amplifier based on voltage combination and balance compensation Marchand Balun. *IEEE Access*. 2018;6: 10131-10138.

[2] Zhu B-H, Kim N-Y, Wang Z-J, Kim E-S. On-chip miniaturized bandpass filter using GaAs-based integrated passive device technology for L-band application. *Materials*. 2019;12 (18):3045.

[3] Liu HW, Lei JH, Zhan X, Guan XH, Ji LY, Ma ZW. Compact quad-band superconducting metamaterial filter based on split ring resonator. *Appl Phys Lett*. 2014;104(22):222602.

[4] Liu HW, Ren BP, Guan XH, Wen P, Wang Y. Quad-band high-temperature superconducting bandpass filter using quadruple-mode square ring loaded resonator. *IEEE Trans Microwave Theory Tech*. 2014;62(12):2931-2941.

[5] Cheng CM, Yang CF. Develop quad-band (1.57/2.45/3.5/5.2 GHz) bandpass filters on the ceramic substrate. *IEEE Microwave Wireless Compon Lett*. 2010;20(5):268-270.

[6] Guo X, Zhu L, Wu W. Design method for multiband filters with compact configuration in substrate integrated waveguide. *IEEE Trans Microwave Theory Tech*. 2018;66(6):3011-3018.

[7] Li XK, Zhang YH, Xu KD, Wang JF, Li SD, Fan Y. Multiband bandpass filter design using E-plane septa for waveguide application. *Microwave Opt Technol Lett*. 2018;60 (10):2367-2370.

[8] Liu JC, Wang JW, Zeng BH, Chang DC. CPW-fed dual-mode double-square-ring resonators for quad-band filters. *IEEE Microwave Wireless Compon Lett*. 2010;20(3):142-144.

[9] Hejazi ZM. A fast design approach of compact microstrip multiband bandpass filters. *Microwave Opt Technol Lett*. 2012;54 (4):1075-1079.

[10] Bukuru D, Song KJ, Zhang F, Zhu Y, Fan MY. Compact quad-band bandpass filter using quad-mode stepped impedance resonator and multiple coupling circuits. *IEEE Trans Microwave Theory Tech*. 2017;65(3):783-791.

[11] Zhang Y, Gao L, Zhang XY. Compact quad-band bandpass filter for DCS/WLAN/WiMAX/5G Wi-fi application. *IEEE Microwave Wireless Compon Lett*. 2015;25(10):645-647.

[12] Luo S, Zhu L. A novel dual-mode dual-band bandpass filter based on a single ring resonator. *IEEE Microwave Wireless Compon Lett*. 2009;19(8):497-499.

[13] Liu HW, Ren BP, Guan XH, Lei JH, Li S. Compact dual-band bandpass filter using quadruple-mode square ring loaded resonator (SRLR). *IEEE Microwave Wireless Compon Lett*. 2013;23(4): 181-183.

[14] Li J, Huang SS, Zhao JZ. Compact dual-wideband bandpass filter using a novel penta-mode resonator (PMR). *IEEE Microwave Wireless Compon Lett*. 2014;24(10):668-670.

[15] Bi XJ, Ma Q, Xu QF, Gui LQ, Li QX. A high-selectivity quad-band bandpass filter utilizing asymmetrical interdigital coupled lines and circular spiral lines. *IEEE Microwave Wireless Compon Lett*. 2018;28(9):792-794.

[16] Wang J, He S, Gan D. A 2.4/3.5/5.2/5.8-GHz quad-band BPF using SLRs and triangular loop resonators. *Electron Lett*. 2018;54 (5):299-301.

[17] Zhang S-X, Qiu L-L, Chu Q-X. Multiband balanced filters with controllable bandwidths based on slotline coupling feed. *IEEE Microwave Wireless Compon Lett.* 2017;27(11):974-976.

[18] Chen JZ, Shen J, Gao N, Zhang AX. Compact quad-band bandpass filter based on sextuple-mode stepped impedance stub-loaded resonator. *Electron Lett.* 2016;52(3):214-215.

[19] Xu J. Compact second-order dual-and quad-band bandpass filters using asymmetrical stub-loaded resonator and uniform-impedance resonator. *Microwave Opt Technol Lett.* 2015;57(4):997-1003.